IEEE Access
Multidisciplinary | Rapid Review | Open Access Journal

Received December 8, 2019, accepted December 19, 2019, date of publication December 23, 2019,
date of current version February 10, 2020.

Digital Object Identifier 10.1109/ACCESS.2019.2961630

Automated Brain Tumor Segmentation Based on Multi-Planar Superpixel Level Features Extracted From 3D MR Images

TAMJID IMTIAZ[1], (Member, IEEE), SHAHRIAR RIFAT[1], (Member, IEEE), SHAIKH ANOWARUL FATTAH[1], (Senior Member, IEEE), AND KHAN A. WAHID[2]

[1]Department of Electrical and Electronic Engineering, Bangladesh University of Engineering and Technology, Dhaka-1205, Bangladesh
[2]Department of Electrical and Computer Engineering, University of Saskatchewan, Saskatoon, SK S7N5A9, Canada

Corresponding author: Khan A. Wahid (khan.wahid@usask.ca)

This work was support by the Natural Sciences and Engineering Research Council of Canada (NSERC).

ABSTRACT Brain tumor segmentation from Magnetic Resonance Imaging (MRI) is of great importance for better tumor diagnosis, growth rate prediction and radiotherapy planning. But this task is extremely challenging due to intrinsically heterogeneous tumor appearance, the presence of severe partial volume effect and ambiguous tumor boundaries. In this work, a unique approach of tumor segmentation is introduced based on superpixel level features extracted from all three planes (*x*-*y*, *y*-*z*, and *z*-*x*) of 3D volumetric MR images. In order to avoid the pixel randomness and to account for precise inhomogeneous boundaries of brain tumor, each of the images belonging to a particular plane is partitioned into irregular patches (superpixels) based on their intensity and spatial similarity. Next, various statistical and textural features are extracted from each superpixel where all three planes are considered separately in order to obtain better labeling on superpixels in tumor edges. A feature selection scheme is proposed based on their performance on histogram based consistency analysis and local descriptor pattern analysis, which offers a significant reduction in feature dimension without sacrificing classification performance. For the purpose of supervised classification, Extremely Randomized Trees is used to classify these superpixels into a tumor or a non-tumor class. Finally, pixel level decision is taken based on corresponding decisions obtained in each plane. Extensive simulations are carried out on publicly available dataset and it is found that the proposed method offers better tumor segmentation performance in comparison to that obtained by some state of the art methods.

INDEX TERMS Magnetic resonance imaging, superpixels, extremely randomized trees, pixel labelling, feature selection, dice score.

I. INTRODUCTION

With the introduction of information technology and advancement in the medical field, accurate segmentation of brain tumors is of the enormous potential for improved diagnosis, growth rate prediction and treatment planning. In the last decade, the immense growth of research interest in processing medical data using machine learning algorithms signifies the importance of this domain [1]–[3]. MRI is the modality of choice for evaluating patients who have symptoms and signs suggesting brain tumor. The nature of brain tumors leads to huge challenges in the development of semi-automated and fully automated brain tumor segmentation method. The variable sizes, positions, and shapes of brain tumors prohibit the use of priors, like shape and location.

In early works, segmentation were often performed based on threshold segmentation algorithms [4], [5], Region-based methods [6]–[8], Edge-based methods [9], [10], Atlas-based methods [11]–[13]. The threshold segmentation method is simple and efficient but due to the high complexity of brain structure and complex boundaries, a threshold-based approach is often used to locate brain tumors [14]. Aneja and Rawat [15] and Zhao *et al.* [16] proposed two different clustering algorithm that works in noisy images. Maoguo et al. [17] proposed an improved Fuzzy C-Means(FCM) algorithm which extended the use of tradeoff weighted fuzzy factor and a kernel metric, the tradeoff weighted fuzzy factor depends on the spatial distance of all neighboring pixels. These methods are not computationally expensive

The associate editor coordinating the review of this manuscript and approving it for publication was Derek Abbott.

but they generally produce poor results and need prior knowledge from experts and feature engineering. Supervised learning-based algorithms use training data labeled by experts for segmentation of tumors Classifiers such as Support Vector Machine [18], [19] was successfully applied in brain tumor segmentation. The RF can handle a multiclass problem with large feature vector. A variety of features were proposed in the literature: encoding context [20]–[22], first-order and fractal-based texture [20], [22]–[25], gradients [20], [23], brain symmetry [20], [23], [27], and physical properties [27]. Geremia *et al.* [25] used discriminative random decision forests to classify the voxels of 3D MRI image for segmentation of tumor. Wu *et al.* [26] used superpixel features in a conditional random fields (CRF) framework to detect brain tumors.

Recently deep learning methods, especially the convolutional neural networks (CNN) have gained popularity among researchers in image classification and biological image segmentation tasks [49], [50]. Zhuge *et. al.* presented holistically nested neural networks which combines multilevel hierarchical intensity representations of the image [51]. Zhao and Jia proposed multiscale CNNs where a three-stream framework can automatically detect the optimum top three scales [52]. Usually, deep neural network based schemes do not need any additional feature extraction stage from data and may provide very high accuracy depending on the proper selection of various tuning parameters. However, it involves high training complexity and a risk of overfitting of the training data.

To implement classical machine learning pipeline like decision trees many aspects are left to be hand engineered. So proper feature selection by detailed analysis, tackling data imbalance present by proper sampling and parameter selection in various cases need extensive reasoning to create a robust and highly accurate segmentation pipeline.

Taking all these challenges into consideration, in this paper, a fully automated brain tumor segmentation scheme is proposed based on superpixel level features extracted from three planes of 3D volumetric MR images from FLAIR, T1c, and T2 modalities of the working dataset. Unlike conventional tumor segmentation methods that consider pixel level or fixed shape block level classification, in the proposed method superpixel based feature extraction along three planes is introduced. Along with the statistical features, Gabor textural features are also extracted. As a classifier, Extremely randomized Trees is used which offers better performance in terms of computational complexity and accuracy in comparison with the other widely used classifiers for this task. Use of superpixels in all three planes helps to avoid partial volume effect and offers better consistency in extracted features even in inhomogenous tumor boundaries of brain tumor. In view of taking the final decision on a pixel, decisions from all three planes are taken into consideration. To demonstrate the segmentation performance, standard BRATS 2013 annotated training dataset is used and various performance parameters are measured.

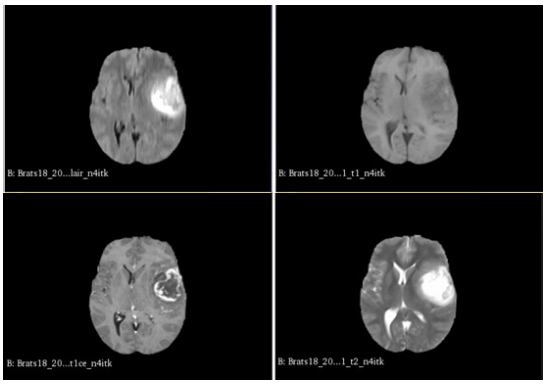

FIGURE 1. Four modalities of brain tumor dataset.

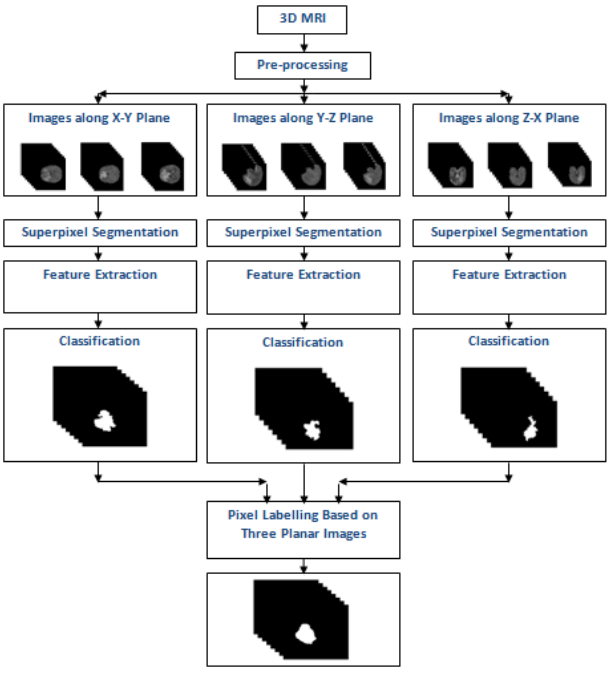

FIGURE 2. Overview of our proposed method.

II. PROPOSED METHOD

In the proposed method, three modalities of MR images namely (FLAIR, T1c, and T2) are used for segmentation purpose. The reason for that is the intensity difference between the tumor and non-tumor region is more prominent in case of FLAIR and T2 images. Non-enhancing tumor core region is hyper-intensified in the T1c images as shown in Fig. 1.

The steps involved in the proposed method are presented in Fig.2. First, an intensity adjustment scheme is applied on the whole 3-D MRI data to reduce the bias in intensities in various types of tissues and a histogram matching algorithm is applied to bring all planar images in a uniform dynamic range. Next, the whole MRI volume is sliced into images along the three planes (x-y, y-z and z-x). Thus, three sets of images are found corresponding to x-y, y-z and z-x planes for a particular modality. Each of the images in a set is partitioned into irregular patches named superpixels based on spatial and

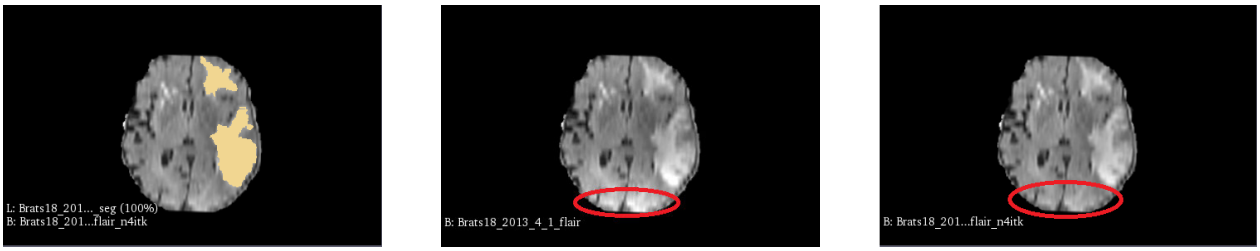

(a) Segmented image (b) Image before MRI bias correction (c) Image after MRI bias correction

FIGURE 3. Effect of MRI bias correction.

intensity similarity. Then from each superpixel, a number of statistical and Gabor Textural features are extracted and the superpixels are then classified using Extremely Randomized Trees (ERT) classifier. Finally, the decision on each pixel is taken considering the labels on the superpixels obtained from all three planes.

A. PREPROCESSING

An MRI volume is a three-dimensional data which can be viewed along with any of the three (x-y, y-z and z-x) directions. The superpixels extracted from images captured from a particular planar direction are different from the scenario when it has been extracted from another plane. The pixels in the most vulnerable areas (edges) of a particular plane might not be edge pixels in other planes. So each 3D MRI of a patient is sliced along three planes and three sets of images are captured for each of the three modalities used in this work.

A bias field is a low frequency smoothly varying undesirable signal that corrupts MR images because of the inhomogeneities in the magnetic field of the MRI machine. Bias field blurs images and thus reduces the high-frequency contents of the image. As a result, similar kind of tissues exhibit different gray level distributions across the image. Hence, the MR images are undergone a bias field correction according to the method presented in [28].

In order to present the effect of bias correction, an MR image segment containing the tumor portion as shown in Fig.3(a). A high-intensity region belonging to the non-tumor portion of the brain image having similar intensity level as the tumor region (visualized in Fig. 3(b)) which can be misclassified by a classifier. But after bias correction, all the tissues have their similar gray level distribution, which is shown in Fig. 3(c).

A major drawback of Magnetic Resonance Imaging is the lack of a standard interpretation of image intensities as the image intensities in MRI do not have a fixed meaning. In view of obtaining a similar dynamic range of MRI pixel intensities a histogram matching algorithm [29] is applied to ensure that all the data have similar dynamic ranges. Histogram of MRI modalities for each of the patients is transformed to match the histogram of the sets of reference images. The reference image set is chosen from the same modality as the transformed image.

As seen from Fig. 4(a), the histograms of the FLAIR modality of patient 1 and patient 2 are transformed from an intensity range of (0-400) and (0-600) to a standard range of (0-200). The similar situation is seen in the other two modalities respectively in Fig. 4(b) and Fig. 4(c).

B. SUPERPIXEL BASED FEATURE EXTRACTION

1) SUPERPIXEL SEGMENTATION

For the segmentation purpose, classifying pixels is a prevalent approach. But for any classifier, this large number of samples is a huge burden. A viable option is to consider a group of pixels and classify the group. In this way, the burden is lessened to a great extent and faster segmentation is achieved. A very common approach is to group the pixels into regular sized patches or blocks and consider them as a unit for extracting features. But due to highly inhomogeneous tumor boundaries of brain tumor fixed sized blocks fails to group the pixels of similar characteristics together and create inconsistency in block features belonging to the same group. Hence, instead of fixed-block, a compact group of pixels with similar characteristics (superpixels) is considered here as the underlying representation. One more advantage of classifying a group of pixels with similar characteristics is that the effect of unwanted random noise on a pixel is relatively high in comparison to that on a compact group of pixels. In order to generate consistent and compact superpixels, the simple linear iterative clustering (SLIC) algorithm [30] is used here which segregates an image into groups with approximately similar characteristics. The major advantage of SLIC method is that it creates groups and there is a very low possibility of grouping pixels of dissimilar characteristics [31]. Moreover, it involves a very low computational cost and a tradeoff is possible between accuracy and classification time. A given image is first divided into equal sized (S) grids and the geometrical center of each grid is considered as the superpixel center. Next, these centers are moved to the seed location corresponding to lowest gradient position in a 3×3 neighbourhood. The pixels in a $2S \times 2S$ neighborhood are clustered together based on two important metrics, spatial and intensity distance metrics. The spatial distance d_s is the geometric distance between a cluster center and a neighboring pixel.The intensity distance metric d_c is taken as the intensity distance of pixels considering all three modalities and calculated

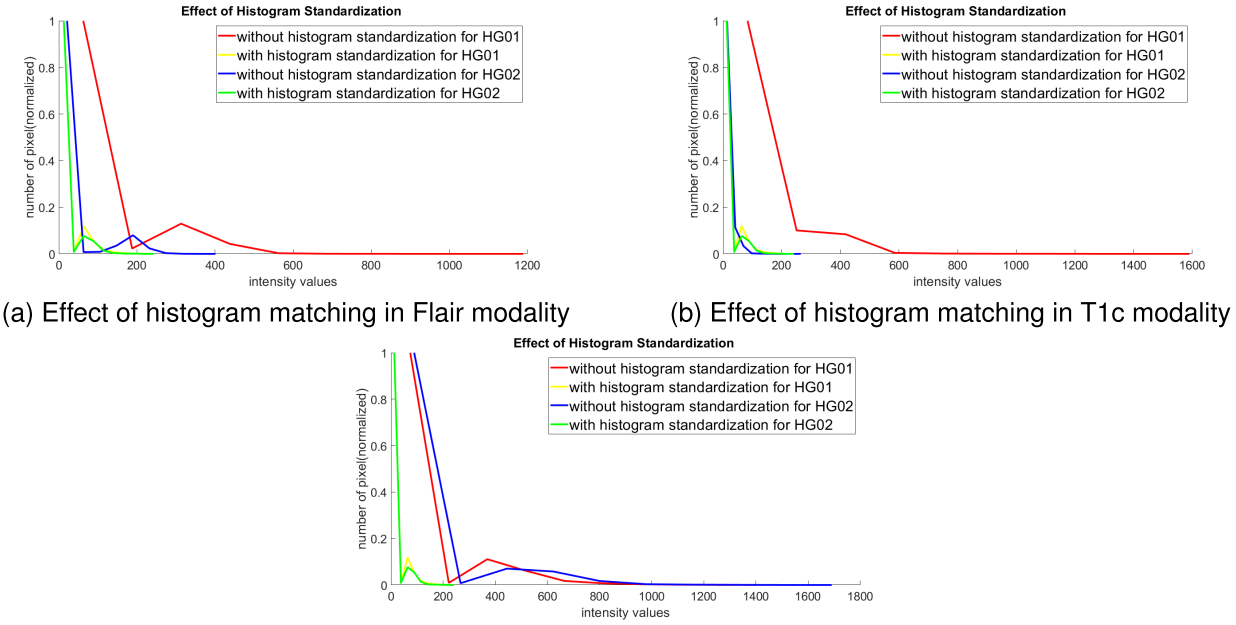

(a) Effect of histogram matching in Flair modality

(b) Effect of histogram matching in T1c modality

(c) Effect of histogram matching in T2 modality

FIGURE 4. Effect of histogram matching algorithm.

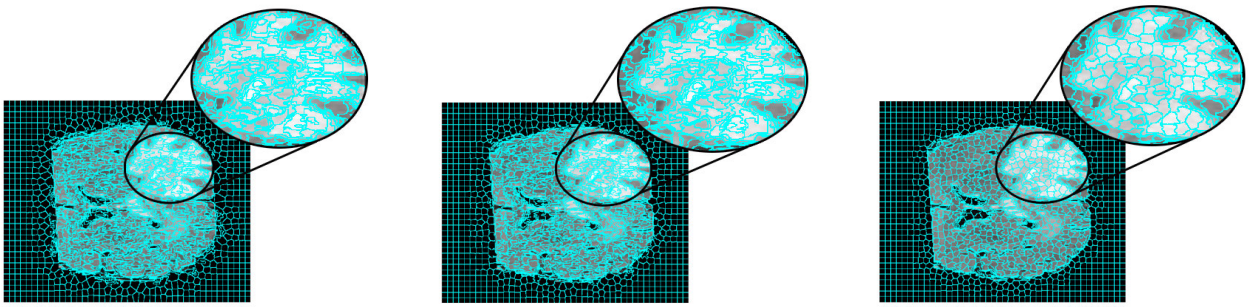

(a) superpixel segmentation using compactness factor m=0

(b) superpixel segmentation using compactness factor m=0.2

(c) superpixel segmentation using compactness factor m=1

FIGURE 5. Visualization of superpixels with different compactness factor m.

as:

$$d_c = \sqrt{(l_{\text{jFlair}} - l_{\text{iFlair}})^2 + (l_{\text{jT1c}} - l_{\text{iT1c}})^2 + (l_{\text{jT2}} - l_{\text{iT2}})^2} \tag{1}$$

where l_{iFlair}, l_{jFlair}, l_{iT1c}, l_{jT1c}, l_{iT2}, and l_{jT2} are the intensity values of the j_{th} cluster center and a neighboring i_{th} pixel of FLAIR, T1c and T2 respectively. Performing superpixel segmentation considering only the intensity of one modality creates inconsistency in the extracted features from other modalities. The overall distance measure, D which is a combination of spatial and intensity distances, is then calculated as:

$$D = \sqrt{d_c^2 + (\frac{d_s}{S})^2 m^2} \tag{2}$$

where m is the compactness coefficient which determines the flexibility of superpixel boundaries. A sample superpixel segmented image is shown in Fig. 5 for different compactness factor, m.

2) STATISTICAL FEATURES

Next, our objective is to represent each superpixel in terms of some representative characteristics. In view of this, a good set of relevant features are required to represent each of these superpixels. Conventionally, statistical features are extracted in most of the cases. But in the proposed method, textural features are extracted along with the statistical features for the proper representation of the superpixels.

Statistical features are computed based on the intensity of the pixels of an object and they express the distribution of grey levels within the sample which are superpixels in

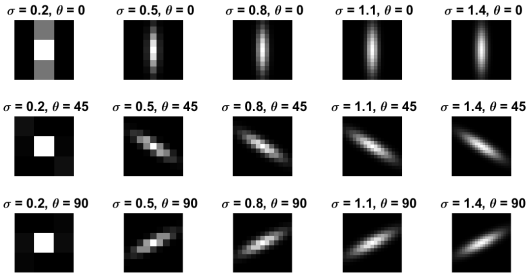

FIGURE 6. **Visualization of Gabor filter in different orientation and filter size.**

this case. Ten statistical features are extracted from each of the superpixels including mean, standard deviation, entropy, mean of absolute deviation, skewness, kurtosis, maximum, minimum, median and mode. A histogram-based consistency analysis is also employed to reduce the number of features which is discussed in II-C.1.

3) TEXTURAL FEATURES

Textural features corresponding to human visual perception are very useful for proper representation of image data. In this proposed method, a Gabor filter bank is used to extract the textural content of the images [45]. The Gabor filter is basically a Gaussian function modulated by complex sinusoid of frequency and orientation and it has the ability to perform both in spatial and frequency domain and can be in any number of dimensions [32], [33].

In the spatial domain, a 2D Gabor filter is a Gaussian kernel function modulated by a sinusoidal plane wave as follows:

$$G(x, y, \theta, \sigma, \lambda, \psi, \gamma) = \frac{\exp(-(x'^2 + \gamma^2 y'^2)}{2\sigma^2} \times \exp(i(\frac{2\pi x'}{\lambda} + \psi)) \quad (3)$$

where $\sigma, \psi, \lambda, \gamma$ are denoted as the filter size, the phase shift, the wavelength and the spatial aspect ratio of sinusoid respectively. x' and y' are calculated from the spatial orientation, θ of the filter by the following equations

$$x' = x\cos\theta + y\sin\theta \quad (4)$$

$$y' = -x\sin\theta + y\cos\theta \quad (5)$$

A set of Gabor filter bank is extracted by varying the filter size σ and orientation θ. Then the filter is convolved with the MR images to obtain the filtered images and mean filter response of pixels within superpixels filtered images is calculated.

C. FEATURE SELECTION

1) SELECTION OF STATISTICAL FEATURES

In most of the previous works [34] [35], a wide range of statistical measures of superpixel are selected but enough reasonings for selecting them is not provided. It is to be noted that all of the statistical measures may not contain significant information to distinguish between classes (tumor and non-tumor class). The statistical features those are used frequently are mean, standard deviation, entropy, mean of absolute deviation, skewness, kurtosis, maximum, minimum, median and mode. To investigate the performance of different statistical features on superpixels of FLAIR, T1c, and T2 images, a histogram based consistency analysis is introduced. First, the total number of superpixels extracted from the whole dataset are selected and divided into Tumor and non-tumor classes according to the pixel level ground truth. Next, the histogram of a feature value for both classes are investigated. In Fig. 7(a-f), histograms of both classes for six features in case of three modalities are shown. Considering the space, all 30 cases are not shown.

It is found that mean, median, mode, maximum and minimum features provide almost distinct separation of tumor and non-tumor class in FLAIR, T1c, and T2 images. On the other hand, for the other features like skewness, kurtosis, entropy, mean of absolute deviation, moment and standard deviation, each of them provides a very similar characteristic and insignificant separation between two classes. As a result, in this work mean, median, mode, maximum and minimum features are selected for their consistent and distinct class separation.

For better understanding, box plots corresponding to the FLAIR, T1c, and T2 modalities considering all the features are presented in Fig. 8(a), Fig. 8(b) and Fig. 8(c) respectively.

2) SELECTION OF TEXTURAL FEATURE'S PARAMETERS

Because of the high variation of tumor in size and shape, five Gabor wavelets of different filter size are used, each with three orientations. The filter size is selected within [0.2 0.5 0.8 1.1 1.4] with increment of 0.3. Initially, eight orientations [0 π/8 2π/8 3π/8 4π/8 5π/8 6π/8 7π/8] are considered. In order to determine the optimal orientation of the Gabor filter from the eight orientations, an orientation analysis is carried out [33]. In this case, the direction at each block of MRI image is determined by eight local direction patterns (LDP) as shown in Fig. 9. The size of these windows is restricted within 3 × 3 block. Every mask pattern is slid over an entire image, convoluted by the LDP operator and pixel values of that image are changed to directional intensities. Finally, eight directional intensities are obtained by summing up the pixel intensities of corresponding blocks. The directional intensity is obtained using the following equations:

$$L_p(i,j) = \sum_{a=-1}^{1}\sum_{b=-1}^{1} f(i+a, j+b) * d_p(a+b) \quad (6)$$

$$L_p = \sum_{i=1}^{m}\sum_{j=1}^{n} L_p(i,j); \quad p = 1, 2, \ldots, 8 \quad (7)$$

$f(i,j)$ in the image is considered as the center of mask pattern and d_p is one of the local patterns. The designed LDP features contain the information of 2-D distribution. Hence, they can represent the image orientation characteristics more closely. The optimal direction of Gabor filter is chosen

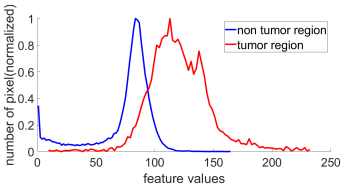

(a) Histogram analysis of 'mean' feature in FLAIR image

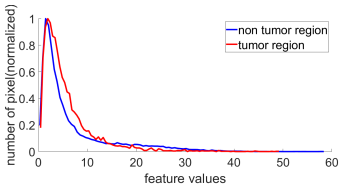

(b) Histogram analysis of 'standard deviation' feature in FLAIR image.

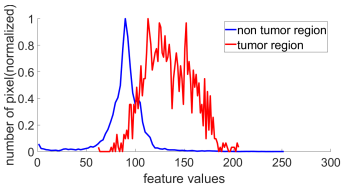

(c) Histogram analysis of 'maximum' feature in T1c image

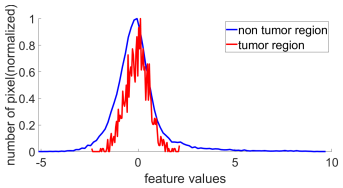

(d) Histogram analysis of 'skewness' feature in T1c image.

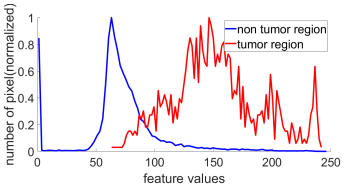

(e) Histogram analysis of 'median' feature in T2 image.

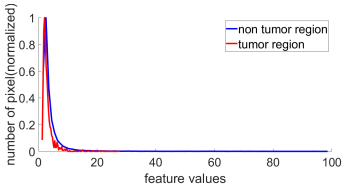

(f) Histogram analysis of 'kurtosis' feature in T2 image.

FIGURE 7. Consistency analysis of statistical features in different modality.

TABLE 1. Dominating no. of images (along *x-y* plane).

Modality	0	$\frac{\pi}{8}$	$\frac{2\pi}{8}$	$\frac{3\pi}{8}$	$\frac{4\pi}{8}$	$\frac{5\pi}{8}$	$\frac{6\pi}{8}$	$\frac{7\pi}{8}$
FLAIR	2649	2247	7	197	774	201	3	2121
T1c	2360	2271	6	539	756	650	3	1605
T2	2393	2304	10	542	854	591	4	1420

TABLE 2. Dominating no. of images (along *y-z* plane).

Modality	0	$\frac{\pi}{8}$	$\frac{2\pi}{8}$	$\frac{3\pi}{8}$	$\frac{4\pi}{8}$	$\frac{5\pi}{8}$	$\frac{6\pi}{8}$	$\frac{7\pi}{8}$
FLAIR	875	1097	7	1539	2801	2040	9	146
T1c	793	1004	64	2241	1590	2586	228	8
T2	1301	184	4	2189	2087	2111	8	630

TABLE 3. Dominating no. of images (along *z-x* plane).

Modality	0	$\frac{\pi}{8}$	$\frac{2\pi}{8}$	$\frac{3\pi}{8}$	$\frac{4\pi}{8}$	$\frac{5\pi}{8}$	$\frac{6\pi}{8}$	$\frac{7\pi}{8}$
FLAIR	2989	746	20	1317	3106	906	3	732
T1c	3238	1284	14	1778	3068	656	4	176
T2	3131	113	15	2504	3355	1003	6	94

considering the larger value of the directional intensity L_p. In this case, the analysis has been applied to the whole image set corresponding to the FLAIR, T1c, and T2 modalities. The directional intensity L_p is calculated for each of the images respectively. For each of the images, the top three values of L_p are chosen which are basically the top three orientation descriptors for that particular image. After analyzing the top three orientation descriptor of all the images, it is found that [0,π/8,7π/8] rank in the top three of most of the images extracted from *x-y* plane corresponding to FLAIR, T1c, and T2 modalities as shown in Table 1. Hence, these orientations are selected for the images extracted from the *x-y* plane. For the same reason, the orientation [3π/8,4π/8,5π/8] are selected for the images extracted from the *y-z* plane and [0,3π/8,4π/8] are selected for the images extracted from the *z-x* plane, which are shown in Table 2 and Table 3, respectively.

For the filter size values under 0.2, filtered images are very close to the original image, while for the values above 1.5, the images are intensively blurred. Therefore, the kernel sizes are selected within this range with the increment of 0.3, i.e. [0.2, 0.5, 0.8, 1.1, 1.4]. Wavelength coefficient $\lambda = 2$ is chosen empirically as It is found out that the value of wavelength has less effect on the performance of the classifier.

After proper feature selection, (5 statistical $\times$ 3 modalities) and (15 textural $\times$ 3 modalities) i.e. 60 features have been selected to create the feature vector.

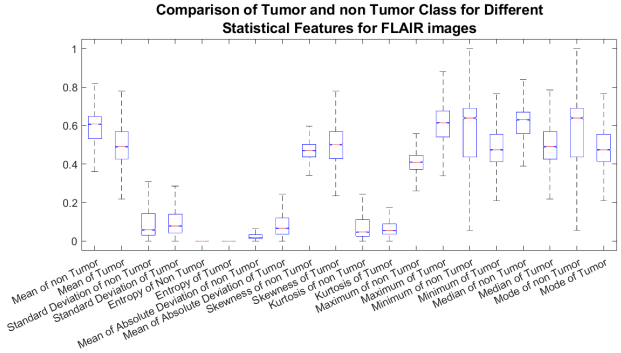

(a) Box Plot of different Statistical Features in FLAIR modality.

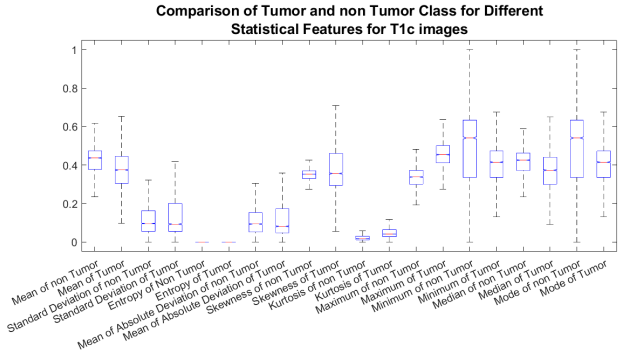

(b) Box Plot of different Statistical Features in T1c modality.

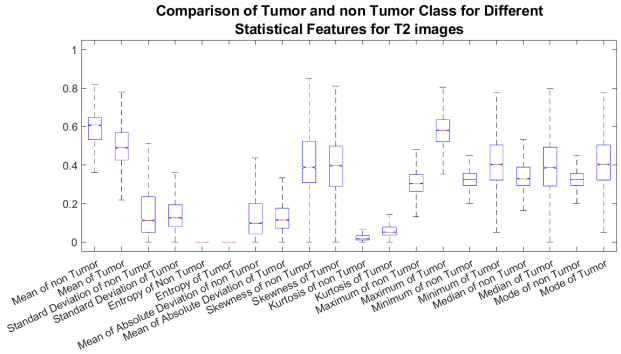

(c) Box Plot of different Statistical Features in T2 modality.

FIGURE 8. Box Plots of different Statistical Features in different modalities.

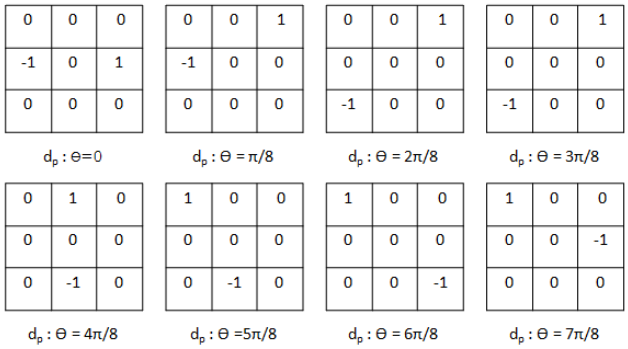

FIGURE 9. Eight local direction patterns(LDPs).

D. EXTREMELY RANDOMIZED TREES CLASSIFIER

The selection of a classifier in a specific machine learning task generally depends on the computational complexity, time, and overfitting of the training datal. Among many classification schemes, Logistic Regression, Support Vector Machine (SVM), Random Forest (RF) and decision-based trees are very popular in different machine learning applications. Among these methods, the Extremely Randomized Trees (ERT), which is a tree-based ensemble method for supervised classification, offers comparably better performance in terms of computational complexity and overfitting of the training data [48]. Besides, it offers the benefit of filtering out the irrelevant features [36]. It randomizes both attributes and cut point choices while splitting a tree node. The strength of randomization of ERT can be controlled by varying the number of trees (M), the strength of attribute randomization (k), and the degree of smoothing (n). Moreover, it comprises of a post-processing stage, in which the tree is cut off based on an independent sample [47]. Hence, it can efficiently remove those parts which can overfit the learning sample. For these reasons, ERT is used as the classifier in this proposed method.

One major concern in the superpixel based supervised classification is the labels of the trainer dataset as the superpixel (Tumor or non-Tumor) is unknown rather the labels of each pixel inside the superpixel are known. As a result, a simple method of assigning the labels of superpixels is proposed in this paper based on the knowledge of pixel-level ground truth. A superpixel is labeled as tumor if the majority of its pixels are marked as tumor pixel as per the ground truth. Due to the inherent property of superpixel formation, there is a tendency of containing pixels with similar nature in a superpixel. Hence, the choice for majority voting for assigning the label of superpixel as tumor or non-tumor to create the training dataset is found satisfactory. For a test superpixel, the features are extracted utilizing three modalities as described in the previous section. Next, the features are fed to the ERT to predict the class label of the test superpixel utilizing the trainer set. It is to be mentioned that all the pixels inside the superpixels are labeled as per the label of the superpixels. This operation is carried out in all the three planes respectively.

E. PIXEL LABELING BASED ON THREE PLANAR VOTING

After classification of superpixels, the images are reconstructed from the classified superpixels and the whole tumor volume is constructed from the images. During the formation of superpixels from a particular planar image, if the tumor region appears very small in shape on that plane, there is a chance of getting false positive cases (non-tumor pixels to be classified as tumor pixels). But when superpixels are extracted from all the three planar images, a good possibility arises that at least in one of them, the tumor may appear to be in better shape than the others. Moreover, it is also possible that the superpixel distribution extracted from a particular

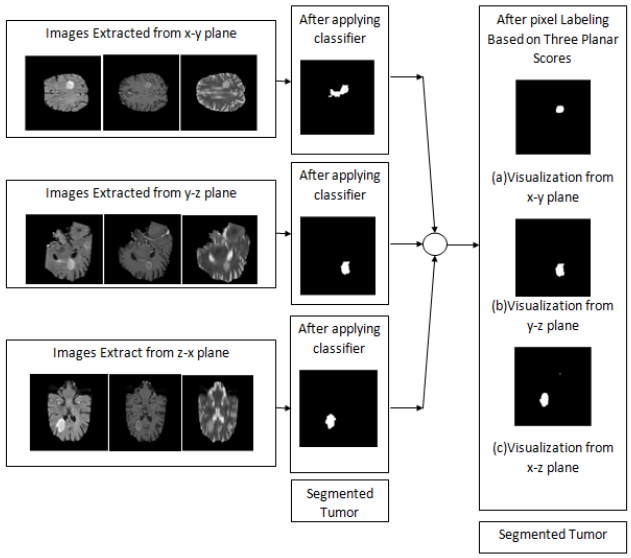

FIGURE 10. Pixel labelling based on three planar score.

plane may have a better boundary separation than the others. For these advantages, the superpixels are extracted from all the three planar images in this proposed method. As a result, each pixel will be assigned a class label (tumor or non-tumor) for three different planes. Finally, a pixel is labeled as Tumor class if the labels obtained from all three planes are found tumor. Otherwise, it is labeled as non-tumor. For better understanding, proposed three planar voting algorithm is demonstrated in Fig. 10. After applying the classifier for segmentation purpose, some false positive cases are found in the first planar image. But, after combining the three planar voting, the false positive cases can be efficiently removed. In the 3-D MRI data, at each spatial location, there will be ultimately one particular class (Tumor or non-Tumor) i.e. the class of each pixel. This three planar votings effectively increases superpixel classification accuracy and also filters out the false positive cases too overall contributing significantly for the accuracy achieved.

III. RESULTS AND ANALYSIS

In proposed method, a two-stage feature extraction technique is applied. In the first stage, two types of features (Statistical and Textural) are extracted from the superpixels extracted from each of the three modalities used in this method. In the next stage, the final feature vector is obtained by concatenating all the features selected from each of the selected modalities. In view of analyzing the quality of these features, statistical and orientational analyses have been performed considering the whole MRI data. Description of the dataset, detailed analysis on the choice of proper parameters, quality of the extracted features and classification performance are presented in the following subsections.

A. DATASET

The brain tumor image data used in this work are obtained from the NCI-MICCAI 2013 Challenge on Multi-modal Brain Tumor Segmentation [37]. Simulation results shown in this section considers 3D MRI volumetric data having manual segmentation for evaluation. The pixel level annotated data are collected from 20 high-grade glioma patients(anaplastic astrocytomas and glioblastoma multiforme tumors) , each one with 4 MRI protocols and the ground truth for each subject. The included protocols are FLAIR, T1, T1c (post-Gadolinium T1) and T2 which differs basically because of their different acquisition procedure.

B. SELECTION OF SUPERPIXEL PARAMETERS

For generating superpixels, two important factors have to be considered. One is compactness of its size and the other is how adherent it is to the boundary or the edge of an image. These two important factors depend on two main parameters of superpixel, which are the initial grid size, S and the compactness coefficient, m. Normally, selecting a larger initial grid size, superpixels of larger areas are generated and less number of superpixels are to be classified. It lessens the burden on the classifier but may hampers the classification accuracy as superpixels of wider areas may have more mislabeled pixels in them. The effect of varying the parameter S is depicted in Fig. 13. Considering overall accuracy and burden on the classifier the initial gird size is selected to be $S = 6$. The compactness coefficient, m is a constant factor by which the value of image intensities is normalized. By default the spatial distance measure is normalized by the initial selection of grid size, S. With the increasing value of m, the intensity distance measures become less dominant for generating superpixels and creates compact superpixels as doing so makes the spatial distance more dominant. In order to improve the boundary adherence of the superpixels, a smaller value of m is selected than its default value 10. But if the intensity measure is made too much dominant (e.g. selecting $m = 0$), the generated superpixels would be of a severely irregular shape giving much importance to the noise present, ignoring spatial proximity. Considering these factors, for initial grid size 6, the value of $m = 1$ is selected by visual inspection which generates superpixels of compact size and good boundary adherence as shown in Fig. 5.

C. SELECTION OF ERT CLASSIFIER PARAMETERS

It is previously mentioned that the ERT classifier has three important parameters on which the performance of the classifier depends. Normally a higher value of K leads to a better chance of filtering out the irrelevant variables. According to [36], the default value of $K = \sqrt{n}$ is optimal for most of the classification problem where n is the total number of features extracted. Hence, $K = 8$ is selected considering the total number of features selected in this method. Next, the degree of smoothing, $n_{\min} = 2$ is considered. As for the number of trees M, it is well known that for randomization methods the behavior of prediction error is a monotonically decreasing function of M. Thus, for values greater than 22 the performance improvement gets saturated. Considering overall computational cost the value of M is selected to be 20.

TABLE 4. Performance comparison in case of single plane and combined plane for 20 HGG patients.

Patient No.	Dice Score (*x*-*y* plane)	Dice Score (*y*-*z* plane)	Dice Score (*z*-*x* plane)	Final Dice Score
HG01	0.76	0.79	0.78	0.82
HG02	0.80	0.75	0.70	0.81
HG03	0.84	0.82	0.83	0.85
HG04	0.81	0.76	0.74	0.84
HG05	0.90	0.87	0.85	0.91
HG06	0.80	0.74	0.81	0.82
HG07	0.84	0.85	0.87	0.89
HG08	0.82	0.75	0.77	0.81
HG09	0.82	0.83	0.76	0.85
HG10	0.78	0.80	0.84	0.85
HG11	0.85	0.87	0.88	0.93
HG12	0.86	0.85	0.81	0.92
HG13	0.79	0.70	0.75	0.81
HG14	0.86	0.92	0.82	0.90
HG15	0.88	0.91	0.90	0.91
HG16	0.84	0.83	0.86	0.88
HG17	0.80	0.79	0.82	0.85
HG18	0.79	0.74	0.70	0.81
HG19	0.81	0.80	0.77	0.82
HG20	0.87	0.82	0.85	0.88
Average	0.826	0.809	0.8055	0.858

TABLE 5. Definition of accuracy measures.

	Tumor	*Non-Tumor*
Tumor	True-Positive(TP)	False-Negative(FN)
Non-Tumor	False-Positive(FP)	True-Negative(TN)

D. EXPERIMENTAL RESULTS

The training and testing are performed with a series of different cross-validations, where the patients are randomly selected into two non-overlapping sets. The performance of the proposed method is determined using five standard performance measures named Dice Coefficient, Sensitivity, Specificity, PPV (Positive Predictive Value) and Jaccard value. Dice Coefficient [40] is the degree of overlap between the system output and the annotation mask obtained from the clinicians. The Dice Coefficient is defined as:

$$\text{Dice} = \frac{2(A \cap B))}{(|\, A + B \,|)} \tag{8}$$

where A and B are the segmented regions found from the model prediction and the ground truth, respectively. Its value varies between 0 and 1 where a higher value indicates higher degree of overlap. In Table 5, definitions of true positive (TP), false negative (FN), false positive (FP), and true negative (TN) are presented. For example, TP corresponds to the event that the test makes a positive prediction, and the subject has a positive result, FP is the event that the test makes a positive prediction, and the subject has a negative result and FN is the event that the test makes a negative prediction, and the subject has a positive result.

TABLE 6. Performance measures on 20 HGG patients.

Patient No.	Specificity	Sensitivity	PPV	Jaccard	Dice Score
HG01	0.94	0.81	0.82	0.72	0.82
HG02	0.92	0.84	0.79	0.74	0.81
HG03	0.95	0.83	0.81	0.75	0.85
HG04	0.99	0.85	0.85	0.72	0.84
HG05	0.98	0.85	0.82	0.73	0.91
HG06	0.99	0.82	0.83	0.72	0.82
HG07	0.99	0.83	0.87	0.77	0.89
HG08	0.93	0.81	0.80	0.78	0.85
HG09	0.99	0.81	0.77	0.65	0.81
HG10	0.95	0.85	0.82	0.78	0.85
HG11	0.99	0.93	0.86	0.82	0.93
HG12	0.94	0.92	0.87	0.81	0.92
HG13	0.87	0.79	0.81	0.75	0.81
HG14	0.95	0.91	0.82	0.79	0.90
HG15	0.99	0.91	0.85	0.80	0.91
HG16	0.99	0.82	0.84	0.75	0.88
HG17	0.95	0.79	0.83	0.75	0.85
HG18	0.94	0.79	0.90	0.72	0.81
HG19	0.93	0.81	0.83	0.71	0.82
HG20	0.97	0.83	0.85	0.75	0.88
Average	0.957	0.840	0.832	0.751	0.858

Sensitivity is defined as

$$\text{Sensitivity} = \frac{\text{TP}}{\text{TP} + \text{FN}} \tag{9}$$

Specificity is defined as

$$\text{Specificity} = \frac{\text{TN}}{\text{TN} + \text{FP}} \tag{10}$$

The positive predictive value (PPV) is defined as

$$\text{PPV} = \frac{\text{TP}}{\text{TP} + \text{FP}} \tag{11}$$

Jaccard Similarity score [46] is defined as

$$\text{Jaccard} = \frac{\text{TP}}{\text{TP} + \text{FP} + \text{FN}} \tag{12}$$

In the proposed method, instead of considering one of the three planes (*x*-*y*, *y*-*z*, *z*-*x*), all three planes are individually considered and then combined. The effect of considering three planes on overall performance is shown in Table 4. Here, the dice scores obtained from each subject in case of considering individual planes (*x*-*y*, *y*-*z*, *z*-*x*) and the proposed three planes are presented separately. Among all sixty cases (20 subjects, 3 individual planes), except for three cases, better classification performance is observed for the proposed combined planes approach.

In order to clearly visualize the tumor segmentation performance, sample images are shown in Fig. 11. Here, the segmented tumor images found after applying the proposed method are depicted. The first row is the 82^{th} slice of HG09 case, the second row is the 80^{th} slice of HG11, and the third row is the 100^{th} slice of HG18. The first three columns present the axial slice of three modalities: FLAIR, T1c and T2. The fourth column presents the segmented results

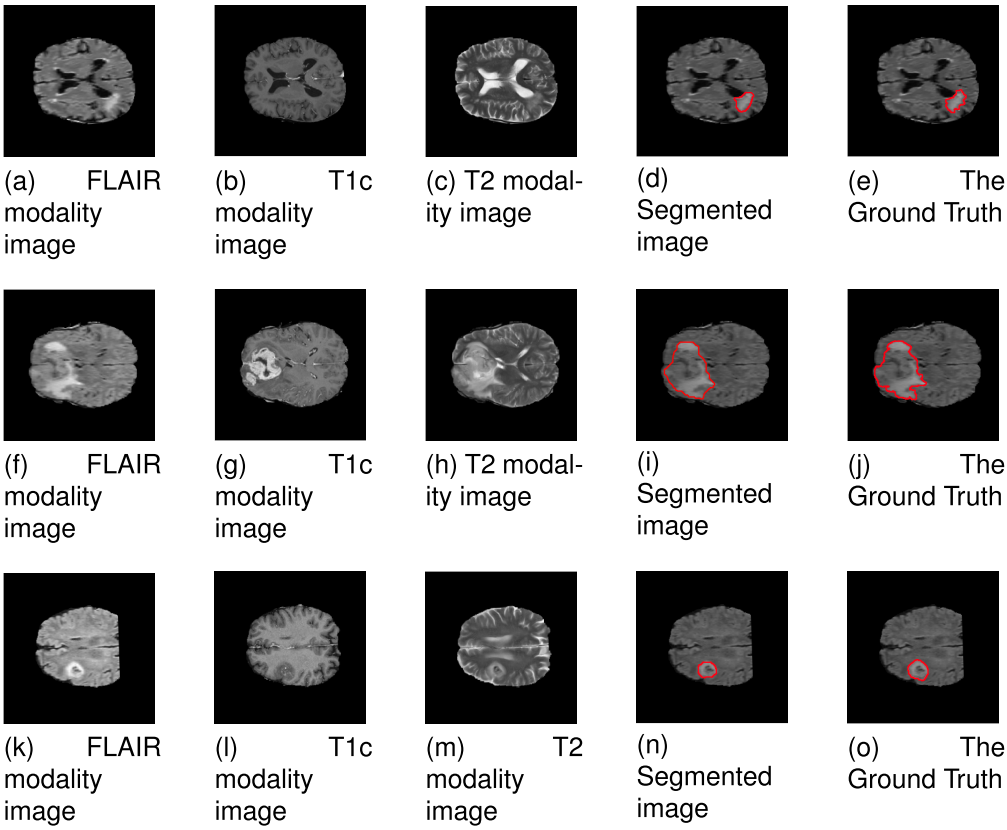

FIGURE 11. Representative segmentation results on one axial slice for three different high-grade subjects (from the first row to the third row) on the real data of the BRATS 2013 data set.

on those axial slices. In the last column, for the purpose of comparison, ground truth image slice is provided. From the figures, one can understand the satisfactory performance of the proposed method.

In table 6, five performance measures, namely Specificity, Sensitivity, PPV, Jaccard and Dice Score are shown considering all 20 subjects. It is observed from these results that a very consistent performance is observed in all cases.

Finally, the performance of the proposed method is compared with that obtained by some other methods reported in [23], [27], [41]–[44], [51], [52]. In different methods, the final classification performance is presented considering various cross validation techniques like leave-one-out, 2-fold, 5-fold or 10-fold cross validations. the performance of the proposed method is evaluated in all these 4 cases of cross validation considering all 20 subjects. In Table 7, performance measures are compared for various methods (as reported in corresponding references). It is evident from these results that the performance of the proposed method is better than that is obtained from these methods in terms of all five performance measures.

In order to compare the computational performance of the proposed method, the computational platform along with the prediction time of different baseline methods are included in Table.8. It is found that the proposed method takes 3.5 minutes to detect tumor for one subject (3.5 minutes/subject), while the method described in [27] takes 100 minutes/subject. Besides, the methods in [23], [41], and [42]have a prediction time of 6, 20, and 30 minutes/subject. The method in [51] has applied a holistically nested neural network for the segmentation purpose which has a prediction time of 30 seconds for each of the images. It is to be noted that the cross validation schemes chosen in different cases vary and thus an exact comparison cannot be performed. However, in general it is found that the proposed method offers satisfactory computational performance in terms of computational time in comparison to that obtained by some existing methods.

E. EFFECT OF PIXEL LABELING BASED ON THREE PLANAR VOTING ON THE PERFORMANCE

In between several layers of 3D MRI, it is expected that a tumor exhibits consistent characteristics inside the tumor boundary unlike the tumor surface where diverse shapes between several layers may be observed. As a result, in the proposed superpixel based classification scheme, a superpixel, which is located inside the tumor boundary, contains mostly tumor pixels. On the other hand, a superpixel located at the tumor surface may contain both tumor and non-tumor pixels in it. If the majority of the pixels in a superpixel exhibits the characteristic of tumor, it is most likely that the superpixel will be classified as tumor class and its pixels are labeled as tumor pixels. Consequently, a redundant region of tumor

TABLE 7. Comparison of proposed method with other approaches.

Approach	Cross validation	Specificity	Sensitivity	PPV	Jaccard	Dice Score
Zhuge [51]	2-fold	-	0.81	-	-	0.78
Zhao [52]	-	-	-	-	-	0.81
Tustison [27]	-	-	0.89	0.85	-	0.87
Cordier [41]	leave-one-out	-	0.78	0.79	-	0.79
Maier [23]	5-fold	-	0.859	0.773	-	0.802
Festa [42]	leave one out	0.87	0.80	-	0.72	0.83
Abbasi [43]	10-fold	-	-	-	0.733	0.837
Banerjee [44]	-	-	-	-	-	0.86
Proposed	2-fold	**0.957**	0.840	0.832	**0.751**	0.858
	5-fold	**0.966**	0.862	**0.851**	**0.79**	0.865
	10-fold	**0.974**	0.88	**0.87**	**0.81**	**0.873**
	leave on out	**0.981**	**0.891**	**0.89**	**0.82**	**0.881**

TABLE 8. Comparison of computational time of different baseline methods.

Method	Computational Platform	Prediction Time
Tustison et. al. [27]	-	100 min (Per Subject)
Zhuge et. al. [51]	DELL PRECISION workstation T7400, NVIDIA Tesla K20c GPU	30 seconds (Per Image)
Festa et.al. [42] [37]	Intel processor (i7- 3930k, 3.2 GHz) and 24 GB of RAM.	30 minutes (Per Subject)
Maier et.al. [23] [37]	-	6 minutes (Per Subject)
Cordier et.al. [41] [37]	-	20 minutes (Per Subject)
Proposed Method	Intel CoreTM i7-8700 3.2 GHz (x12) processor, 8 GB of RAM	Approximately 3.5 minutes (Per Subject)

pixels is introduced in the outer surface region. On the other hand, non-tumor dominated superpixel will be classified as non-tumor class and its pixels are labeled as non-tumor pixels resulting in losing some tumor pixels. As a result, according to the three planar voting approach, two possible cases are observed in the outer surface: a tumor pixel if misclassified as a non-tumor in any one of the three planes will be discarded and at the same time, a non tumor pixel if misclassified as tumor pixel will also be discarded. In general, the second case is mostly observed in outer surface of tumor region which helps in removing non tumor regions in the predicted tumor region. The possible alternate to the current three planar voting approach - single planar voting (a pixel is labeled as Tumor class if the label obtained from at least one plane is found tumor) and double planar voting (a pixel is labeled as Tumor class if the labels obtained from at least two planes are found tumor) are also considered and evaluated in the BRATS 2013 database. As in the single planar voting the pixel is labeled as tumor if it is declared as tumor by at least one of the planar scores, there is less possibility to discard any tumor pixel which is usually happenened in the outer surface superpixel as discussed previously. Hence the single planar voting has an advantage over the current voting approach in that particular case and eventually increases the sensitivity in most of the cases as shown in Table.9. However, the main problem of this approach is that it includes a huge redundant tumor region created from the pixel labeling - based on superpixel label in all the three planar classification individually. This situation is illustrated in Fig.12. where a random patients' data is evaluated and it is found that in the single planar voting approach, the tumor region is larger in comparison with the original tumor region. Consequently, the dice score measured is severely affected as it is depend on the segmented region. In the dice score measure (8), if the segmented region (B) is bigger than the original tumor (A), the overall volume ($A+B$) is increased drastically, resulting in a degradation of dice score performance. The similar situation is happened in the double planar voting approach. On the other hand, the current three planar voting approach has the advantage to discard the redundant region by forcing the labeling of a pixel to be determined by all the three planar scores. As a result, though sensitivity is sacrificed, the overall performance is improved by the three planar voting approach.

F. PERFORMANCE COMPARISON BETWEEN EXTREMELY RANDOMIZED TREES AND OTHER CLASSIFIERS

In order to visualize the computational complexity of different classification schemes, Table.10 is included, where order of the training complexity as well as training time is reported. The parameters used in representing the order of training computational complexity (denoted as $O(.)$) are:

- n is the number of training samples,
- d is the number of features,
- c is the number of class,

TABLE 9. Effect of different voting schemes on performance measures.

Patient No.	Single Planar Voting			Double Planar Voting			Three Planar Voting		
	Specificity	Sensitivity	Dice Score	Specificity	Sensitivity	Dice Score	Specificity	Sensitivity	Dice Score
HG01	0.96	0.93	0.51	0.97	0.78	0.68	0.94	0.81	0.82
HG02	0.98	0.82	0.47	0.96	0.92	0.72	0.92	0.84	0.81
HG03	0.99	0.95	0.69	0.99	0.91	0.68	0.95	0.83	0.85
HG04	0.95	0.93	0.68	0.98	0.90	0.65	0.99	0.85	0.84
HG05	0.92	0.81	0.51	0.97	0.87	0.78	0.98	0.85	0.91
HG06	0.99	0.92	0.64	0.98	0.98	0.69	0.99	0.82	0.82
HG07	0.95	0.93	0.57	0.95	0.92	0.72	0.99	0.83	0.89
HG08	0.98	0.94	0.68	0.97	0.93	0.76	0.93	0.81	0.85
HG09	0.97	0.97	0.45	0.99	0.93	0.72	0.99	0.81	0.81
HG10	0.99	0.88	0.47	0.98	0.95	0.72	0.95	0.85	0.85
HG11	0.98	0.98	0.78	0.99	0.96	0.88	0.99	0.93	0.93
HG12	0.91	0.97	0.67	0.98	0.82	0.85	0.94	0.92	0.92
HG13	0.98	0.73	0.66	0.99	0.64	0.70	0.87	0.79	0.81
HG14	0.97	0.91	0.52	0.95	0.77	0.79	0.95	0.91	0.90
HG15	0.99	0.92	0.68	0.93	0.92	0.81	0.99	0.91	0.91
HG16	0.98	0.92	0.78	0.99	0.82	0.86	0.99	0.82	0.88
HG17	0.96	0.83	0.54	0.96	0.92	0.73	0.95	0.79	0.85
HG18	0.97	0.73	0.57	0.99	0.82	0.68	0.94	0.79	0.81
HG19	0.97	0.99	0.57	0.99	0.95	0.80	0.93	0.81	0.82
HG20	0.99	0.94	0.72	0.97	0.84	0.79	0.97	0.83	0.88

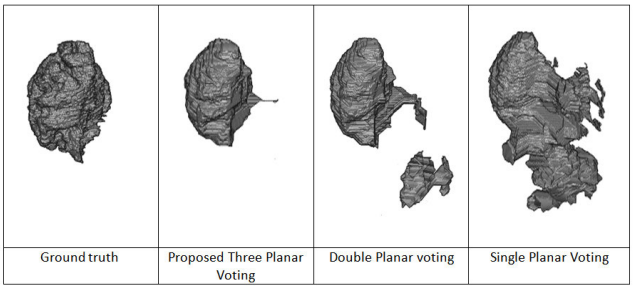

FIGURE 12. (From Left to Right) 3-D view of Actual Tumor Region of HG11 patient, Tumor region extracted from three planar voting, Tumor region extracted from double planar voting, Tumor region extracted from single planar voting.

- E is the number of epoch in training,
- M is the number of trees, and
- k is a constant (where $d \gg k$).

In Table.10, along with the order of training computational complexity, training time required by the classifiers and classification performance in terms of dice score under a similar testing condition are also reported. Among the classifiers mentioned above, except Logistic Regression, other classifiers exhibit competitive classification performance. However, in case of large number training samples like in the current application, the number of samples (n) is much higher than the number of trees and number of features, which eventually increases the computational complexity as well as computational time of SVM and RF classifiers in comparison to the ERT classifier. In this example, in order to evaluate the performance of a neural network, a four-layer feed-forward neural network is implemented. The number of neurons in the two hidden layers is chosen to be 40 and 20, respectively, which gives better classification accuracy. The weights of the network are adjusted by a back-propagation procedure with an adaptive learning rate to obtain the desired output. The tan-sigmoid and softmax activation functions were used for the hidden layers and final output layers, respectively. Applying the network, it is found that a classification accuracy very closer to the ERT classifier is achieved. Yet, considering the complexity of tuning different parameters and training complexity of the neural network, the ERT is chosen in the proposed method. Here, the computational performance analysis is carried out on Intel CoreTM i7-8700 3.2 GHz (x12) processor, 8 GB of RAM, running on Windows 10 64 bit OS. Classifiers used here for comparison are implemented using MATLAB and the codes used here are not fully optimized.

TABLE 10. Computational complexity of different algorithms.

Algorithm	Training Complexity	Traning Time(sec)	Dice Score
Logistic Regression	$O((d+1)cnE)$	491	0.76
SVM	$O(n^3)$	1820	0.823
RF	$O(Mdnlogn)$	524	0.849
ERT	$O(Mknlogn)$	**335**	**0.858**
ANN	-	7200	0.838

G. PERFORMANCE COMPARISON BETWEEN SUPERPIXEL AND FIXED BLOCK BASED IMAGE PARTITION

Fixed block of pixels or sliding window has been used as an alternative of superpixel in many object detection and image segmentation tasks. In [38], [39], the image is partitioned into fixed block of sliding windows and features are extracted from these blocks. But due to the arbitrary shape of the Tumor, a fixed block window does not provide proper information about the edge portions of a tumor region. It is

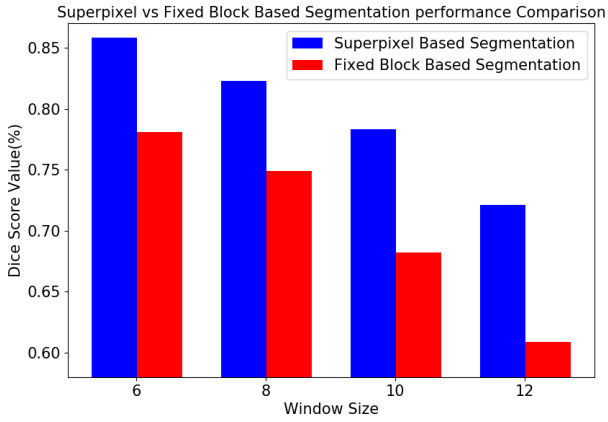

FIGURE 13. **Performance comparison between superpixel and fixed block based image partition.**

because at the edge the block may contain both types of pixels (tumor and non-tumor), which creates severe mislabeling in classification. But in the case of superpixel, the whole image is divided into non-overlapping and uneven blocks according to their intensity similarity. Consequently, the edge portion is precisely preserved and the performance of superpixels dominates over the fixed block. In Fig. 13, considering the same window size, performance obtained by the proposed method in case of superpixel and fixed block is presented. Here, average dice score value is considered as a performance index. The performance reported here is the average dice value obtained from all 20 subjects. It is clearly observed from the figure that the performance with superpixels is much better than that obtained using fixed blocks irrespective of the window sizes. As discussed before (section III-B), with superpixels of larger size the chance of inclusion of more dissimilar pixels increases thus classification performance may degrade. This fact is also clearly observed in Fig. 13.

IV. CONCLUSION

In this paper, a tumor segmentation method based on three planar superpixel features extracted from the 3-D MRI data is introduced. In order to tackle the problem of planar data imbalance and mislabeling of the pixels present in a certain plane which is inherent in slice wise detection of the tumor, three planar superpixel based statistial and textural features extraction is performed. Unlike conventional feature based methods, where a large number of features are considered, we propose to utilize five statistical features those were shown to be more effective in obtaining large class separation. An exhaustive analysis for finding the suitable feature set is done which not only contribute to the accuracy but also reduce computational burden. For selecting the optimum Gabor orientation, a rank based orientation selection method is applied by analyzing the whole MR images. Performing pixel labeling based on three planar images, it is found that considering all three planar images for segmentation enhances the classification performance of the task. The proposed method is evaluated on a publicly available dataset and it offers excellent segmentation performance in comparison to some existing methods in terms of Sensitivity, Specificity, PPV, Jaccard Score and Dice coefficient.

It is observed that the proposed method offers comparatively better performance in terms of various performance measures. However, considering very high level of precision in tumor region segmentation, further increase in values of performance metrices is desired. One possible future work could be to investigate the performance of various neural network based schemes, such as deep neural network or convolutional neural network. In that case, large number of labeled training data is required to train the complex models, which is not always available for medical applications and computational complexity needs to be sacrificed.

REFERENCES

[1] C. Ma, G. Luo, and K. Wang, "Concatenated and connected random forests with multiscale patch driven active contour model for automated brain tumor segmentation of MR images," *IEEE Trans. Med. Imag.*, vol. 37, no. 8, pp. 1943–1954, Aug. 2018.

[2] A. Pinto, S. Pereira, H. Dinis, C. A. Silva, and D. M. L. D. Rasteiro, "Random decision forests for automatic brain tumor segmentation on multi-modal MRI images," in *Proc. IEEE 4th Portuguese Meeting Bioeng. (ENBENG)*, Feb. 2015, pp. 1–5.

[3] V. Pedoia, S. Balbi, and E. Binaghi, "Fully automatic brain tumor segmentation by using competitive EM and graph cut," in *Proc. Int. Conf. Image Anal. Process.* Cham, Switzerland: Springer, 2015, pp. 568–578.

[4] A. Stadlbauer, E. Moser, S. Gruber, R. Buslei, C. Nimsky, R. Fahlbusch, and O. Ganslandt, "Improved delineation of brain tumors: An automated method for segmentation based on pathologic changes of 1H-MRSI metabolites in gliomas," *Neuroimage*, vol. 23, no. 2, pp. 454–461, 2004.

[5] P. Gibbs, D. L. Buckley, S. J. Blackband, and A. Horsman, "Tumour vol. determination, from MR images by morphological segmentation," *Phys. Med. Biol.*, vol. 41, no. 11, pp. 24–37, 1996.

[6] M. R. Kaus, S. K. Warfield, A. Nabavi, P. M. Black, F. A. Jolesz, and R. Kikinis, "Automated segmentation of MR images of brain tumors," *Radiology*, vol. 218, no. 2, pp. 586–591, 2001.

[7] J. E. Cates, R. T. Whitaker, and G. M. Jones, "Case study: An evaluation of user-assisted hierarchical watershed segmentation," *Med. Image Anal.*, vol. 9, no. 6, pp. 566–578, 2005.

[8] M. M. Letteboer, O. F. Olsen, E. B. Dam, P. W. Willems, M. A. Viergever, and W. J. Niessen, "Segmentation of tumors in magnetic resonance brain images using an interactive multiscale watershed algorithm," *Acad. Radiol.*, vol. 11, no. 10, pp. 1125–1138, 2004.

[9] V. Caselles, F. Catté, T. Coll, and F. Dibos, "A geometric model for active contours in image processing," *Numer. Math.*, vol. 66, no. 1, pp. 1–31, 1993.

[10] J. E. Cates, A. E. Lefohn, and R. T. Whitaker, "Gist: An interactive, GPU-based level set segmentation tool for 3D medical images," *Med. Image Anal.*, vol. 8, no. 3, pp. 217–231, 2004.

[11] B. H. Menze, K. V. Leemput, D. Lashkari, M. A. Weber, N. Ayache, and P. Golland, "A generative model for brain tumor segmentation in multi-modal images," in *Proc. Int. Conf. Med. Image Comput. Comput.-Assist. Intervent.* Beijing, China: Springer, 2010, pp. 151–159.

[12] N. Moon, E. Bullitt, K. V. Leemput, and G. Gerig, "Model-based brain and tumor segmentation," in *Proc. IEEE 16th Int. Conf. Pattern Recognit.*, Aug. 2002, pp. 528–531.

[13] M. Prastawa, E. Bullitt, N. Moon, K. Van Leemput, and G. Gerig, "Automatic brain tumor segmentation by subject specific modification of atlas priors," *Acad. Radiol.*, vol. 10, no. 12, pp. 1341–1348, 2003.

[14] M. S. Atkins and B. T. Mackiewich, "Fully automatic segmentation of the brain in MRI," *IEEE Trans. Med. Imag.*, vol. 17, no. 1, pp. 98–107, Feb. 1998.

[15] D. Aneja and T. K. Rawat, "Fuzzy clustering algorithms for effective medical image segmentation," *Int. J. Int. Syst.*, vol. 11, pp. 55–61, Oct. 2013.

[16] F. Zhao, H. Liu, and J. Fan, "A multiobjective spatial fuzzy clustering algorithm for image segmentation," *Appl. Soft Comput.*, vol. 30, pp. 48–57, May 2015.

[17] G. Maoguo, L. Yan, S. Jiao, M. Wenping, and M. Jingjing, "Fuzzy C-means clustering with local information and kernel metric for image segmentation," *IEEE Trans. Image Process.*, vol. 22, no. 2, pp. 2055–2058, Feb. 2013.
[18] S. Bauer, L. P. Nolte, and M. Reyes, "Fully automatic segmentation of brain tumor images using support vector machine classification in combination with hierarchical conditional random field regularization," in *Medical Image Computing and Computer-Assisted Intervention—MICCAI*. New York, NY, USA: Springer, 2011, pp. 354–361.
[19] C.-H. Lee, S. Wang, A. Murtha, M. R. G. Brown, and R. Greiner, "Segmenting brain tumors using pseudo–conditional random fields," in *Medical Image Computing and Computer-Assisted Intervention—MICCAI*. New York, NY, USA: Springer, 2008, pp. 359–366.
[20] R. Meier, S. Bauer, J. Slotboom, R. Wiest, and M. Reyes, "Appearance-and context-sensitive features for brain tumor segmentation," in *Proc. MICCAI Brain Tumor Segmentation Challenge (BraTS)*, 2014, pp. 20–26.
[21] D. Zikic, B. Glocker, E. Konukoglu, A. Criminisi, C. Demiralp, J. Shotton, O. M. Thomas, T. Das, R. Jena, and S. J. Price, "Decision forests for tissue-specific segmentation of high-grade gliomas in multi-channel MR," in *Medical Image Computing and Computer-Assisted Intervention—MICCAI*. New York, NY, USA: Springer, 2012, pp. 369–376.
[22] A. Pinto, "Brain tumour segmentation based on extremely randomized forest with high-level features," in *Proc. IEEE 37th Annu. Int. Conf. (EMBC)*, Aug. 2015, pp. 3037–3040.
[23] R. Meier, "A hybrid model for multimodal brain tumor segmentation," in *Proc. NCI-MICCAI BRATS*, 2013, pp. 31–37.
[24] S. Reza and K. Iftekharuddin, "Multi-fractal texture features for brain tumor and edema segmentation," *Proc. SPIE, Med. Imag. Int. Soc. Opt. Photon.*, vol. 9035, Mar. 2014, Art. no. 903503.
[25] E. Geremia, O. Clatz, B. H. Menze, E. Konukoglu, A. Criminisi, and N. Ayache, "Spatial decision forests for MS lesion segmentation in multi-channel magnetic resonance images," *NeuroImage*, vol. 57, no. 2, pp. 378–390, 2011.
[26] W. Wu, A. Y. C. Chen, L. Zhao, and J. J. Corso, "Brain tumor detection and segmentation in a CRF (conditional random fields) framework with pixel-pairwise affinity and superpixel-level features," *Int. J. Comput. Assist. Radiol. Surgery*, vol. 9, no. 2, pp. 241–253, 2014.
[27] N. J. Tustison, K. Shrinidhi, M. Wintermark, C. R. Durst, B. M. Kandel, J. C. Gee, M. C. Grossman, and B. B. Avants, "Optimal symmetric multimodal templates and concatenated random forests for supervised brain tumor segmentation (simplified) with ANTsR," *Neuroinformatics*, vol. 13, no. 2, pp. 209–225, Apr. 2015.
[28] N. J. Tustison, B. B. Avants, P. A. Cook, Y. Zheng, A. Egan, P. A. Yushkevich, and J. C. Gee, "N4ITK: Improved N3 bias correction," *IEEE Trans. Med. Imag.*, vol. 29, no. 6, pp. 20–1310, Jun. 2010.
[29] L. G. Nyul, J. K. Udupa, and X. Zhang, "New variants of a method of MRI scale standardization," *IEEE Trans. Med. Imag.*, vol. 19, no. 2, pp. 143–150, Feb. 2000.
[30] R. Achanta, A. Shaji, K. Smith, A. Lucchi, P. Fua, and S. Süsstrunk, "SLIC superpixels compared to state-of-the-art superpixel methods," *IEEE Trans. Pattern Anal. Mach. Intell.*, vol. 34, no. 11, pp. 2274–2282, Nov. 2012.
[31] J. E. Vargas-Muñoz, A. S. Chowdhury, E. B. Alexandre, F. L. Galvão, P. A. V. Miranda, and A. X. Falcão, "An iterative spanning forest framework for superpixel segmentation," *IEEE Trans. Image Process.*, vol. 28, no. 7, pp. 3477–3489, Jul. 2019.
[32] T. S. Lee, "Image representation using 2D Gabor wavelets," *IEEE Trans. Pattern Anal. Mach. Intell.*, vol. 18, no. 10, pp. 959–971, Oct. 1996.
[33] W.-Y. Han and J.-C. Lee, "Palm vein recognition using adaptive Gabor filter," *Expert Syst. Appl.*, vol. 39, no. 18, pp. 13225–13234, Dec. 2012.
[34] S. Pereira, J. Festa, J. A. Mariz, N. Sousa, and C. A. Silva, "Automatic brain tissue segmentation of multi-sequence MR images using random decision forests," in *Proc. MICCAI Grand Challenge MR Brain Image Segmentation (MRBrainS13)*, 2013.
[35] M. Soltaninejad, G. Yang, T. Lambrou, N. Allinson, T. L. Jones, T. R. Barrick, F. A. Howe, and X. Ye, "Automated brain tumour detection and segmentation using superpixel-based extremely randomized trees in flair MRI," *Int. J. Comput. Assist. Radiol. Surgery*, vol. 12, no. 2, pp. 183–203, 2017.
[36] P. Geurts, D. Ernst, and L. Wehenkel, "Extremely randomized trees," *Mach. Learn.*, vol. 63, no. 1, pp. 3–42, 2006.
[37] B. H. Menze *et al.*, "The multimodal brain tumor image segmentation benchmark (BRATS)," *IEEE Trans. Med. Imag.*, vol. 34, no. 10, pp. 1993–2024, 2015.
[38] N. Nabizadeh and M. Kubat, "Brain tumors detection and segmentation in MR images: Gabor wavelet vs. statistical features," *J. Comput. Elect. Eng.*, vol. 45, pp. 286–301, Jul. 2015.
[39] L. Yanyun and S. Zhijian, "Automated brain tumor segmentation in magnetic resonance imaging based on sliding-window technique and symmetry analysis," *Chin. Med. J.*, vol. 127, no. 3, pp. 462–468, 2014.
[40] L. R. Dice, "Measures of the amount of ecologic association between species," *Ecology*, vol. 26, no. 3, pp. 297–302, 1945.
[41] N. Cordier, B. Menze, H. Delingette, and N. Ayache, "Patch-based segmentation of brain tissues," in *Proc. EEE MICCAI Challenge Multimodal Brain Tumor Segmentation*, 2013, pp. 6–17.
[42] J. Festa, S. Pereira, J. Mariz, N. Sousa, and C. Silva, "Automatic brain tumor segmentation of multi-sequence MR images using random decision forests," in *Proc. BraTS-MICCAI*, 2013, pp. 23–26.
[43] S. Abbasi and F. Tajeripour, "Detection of brain tumor in 3D MRI images using local binary patterns and histogram orientation gradient," *Neurocomputing*, vol. 219, pp. 526–535, Jan. 2017.
[44] S. Banerjee, S. Mitra, and B. U. Shankar, "Automated 3D segmentation of brain tumor using visual saliency," *Inf. Sci.*, vol. 424, no. C, pp. 337–353, Jan. 2018.
[45] D. Gabor, "Theory of communication, Part 1: The analysis of information," *J. Inst. Electr. Engineers III, Radio Commun. Eng.*, vol. 93, no. 26, pp. 429–441, 1946.
[46] P. Jaccard, "The distribution of the flora in the alpine zone.1," *New Phytologist*, vol. 11, no. 2, pp. 37–50, Feb. 1912.
[47] L. Wehenkel, D. Ernst, and P. Geurts, "Ensembles of extremely randomized trees and some generic applications," in *Proc. Robust Methods Power Syst. State Estimation Load Forecasting*, 2006.
[48] W. Czarnecki, S. Podlewska, and A. Bojarski, "Extremely randomized machine learning methods for compound activity prediction," *Molecules*, vol. 20, no. 11, pp. 20107–20117, 2015.
[49] N. Liu, L. Wan, Y. Zhang, T. Zhou, H. Huo, and T. Fang, "Exploiting convolutional neural networks with deeply local description for remote sensing image classification," *IEEE Access*, vol. 6, pp. 11215–11228, 2018.
[50] Y. Bengio, A. Courville, and P. Vincent, "Representation learning: A review and new perspectives," *IEEE Trans. Pattern Anal. Mach. Intell.*, vol. 35, no. 8, pp. 1798–1828, Aug. 2013.
[51] Y. Zhuge, A. V. Krauze, H. Ning, J. Y. Cheng, B. C. Arora, K. Camphausen, and R. W. Miller, "Brain tumor segmentation using holistically nested neural networks in MRI images," *Med. Phys.*, vol. 44, no. 10, pp. 5234–5243, 2017.
[52] L. Zhao and K. Jia, "Multiscale CNNs for brain tumor segmentation and diagnosis," *Comput. Math. Methods Med.*, vol. 2016, Mar. 2016, Art. no. 8356294.

TAMJID IMTIAZ received the B.Sc. degree from the EEE Department, Bangladesh University of Engineering and Technology. He is currently pursuing the M.Sc. degree in electrical and electronic engineering with the Bangladesh University of Engineering and Technology. His research interest lies in biomedical signal processing, image processing, machine learning and computer vision.

SHAHRIAR RIFAT received the B.Sc. degree from the EEE Department, Bangladesh University of Engineering and Technology. He is currently pursuing the M.Sc. degree with the EEE Department. His research interest lies in biomedical signal processing, image processing, machine learning, and deep learning.

SHAIKH ANOWARUL FATTAH received the B.Sc. and M.Sc. degrees from BUET, Bangladesh, and the Ph.D. degree in ECE from Concordia University, Canada. He held a visiting postdoctoral position and later a Visiting Research Associate at Princeton University, USA. He has been serving as a Professor with the Department of EEE, BUET. He has published more than 170 international journal article and conference papers with some best paper awards. His major research interests include biomedical engineering and signal processing. He is regularly delivering Keynote/Invited/Visiting Talks in many countries. He is also a Fellow of IEB. He is also a Committee Member of IEEE PES (LRPC), IEEE EAB (CEC), IEEE SSSIT (SDHTC), IEEE SIGHT (2016 EAC), and 2018 IEEE HAC and R10. He was a recipient of the 2016 IEEE MGA Achievement Award and the 2017 IEEE R10 Humanitarian Technology Activity Outstanding Volunteer Award. He received several prestigious awards, such as the Concordia Universitys' Distinguished Doctoral Dissertation Prize in ENS, the Dr. Rashid Gold Medal (M.Sc., BUET), the NSERC Postdoctoral Fellowship, the URSI Canadian Young Scientist Award 2007, and the BAS-TWAS Young Scientists Prize 2014. He is also the General Chair of the IEEE R10 HTC2017, the TPC Chair of the IEEE WIECON-ECE 2016 and 2017, the MediTec 2016, IEEE ICIVPR 20017, and the ICAEE 2017. He was the Chair of IEEE Bangladesh Section from 2015 to 2016, where he was also the Chair of the 2017 IEEE EMBS Bangladesh Chapter and a Founder Chair of IEEE RAS. He was the Editor of Journal of EE and IEB. He is also the Editor of the IEEE PES Enews and an Associate Editor of the IEEE Access and CSSP (Springer).

KHAN A. WAHID received the B.Sc. degree in electrical and electronic engineering from the Bangladesh University of Engineering and Technology, Dhaka, Bangladesh, in 2000, and the M.Sc. and Ph.D. degrees in electrical and computer engineering from the University of Calgary, Calgary, AB, Canada, in 2003 and 2007, respectively. He is currently a Professor with the Department of Electrical and Computer Engineering, University of Saskatchewan, Saskatoon, SK, Canada. He has coauthored two book chapters and more than 140 peer-reviewed journal and international conference papers in the field of video and image processing, embedded systems, the Internet of Things, medical imaging, and health informatics. He holds two patents. He has received many prestigious awards and scholarships, including the Most Distinguished Killam Scholarship and the NSERC Canada Graduate Scholarship for his Ph.D. research, along with the Award of Innovation from Innovation Place, in 2016. He is also a Registered Professional Engineer in the Province of Saskatchewan.